

Research on the Corrosion Behavior of Q295GNH and Q390GNH Weathering Steels in a Simulated Marine Atmospheric Environment

Shuliang Wang^{1,2,*}, Ping Hu^{1,2}, Zekun Liu², Jie Yan², Wanneng Lei³, Yongbing Liu¹

¹ State Key Laboratory of Oil and Gas Reservoir Geology and Exploitation, Southwest Petroleum University, Chengdu 610500, China.

² School of New Energy and Materials, Southwest Petroleum University, Chengdu 610500, China

³ Oil & Gas Field Productivity Construction Department, Tarim Oilfield Company, Korla 841000, China.

*E-mail: wsliang1465@126.com

Received: 26 July 2022 / Accepted: 2 October 2022 / Published: 20 October 2022

A salt fog corrosion test is designed, and weight loss, XRD, SEM, EDS, and electrochemical testing methods are adopted to study the Q295GNH and Q390GNH weathering steels when simulating the ocean atmospheric environment. The results show that during corrosion, the Q295GNH weathering steel undergoes uniform corrosion, and the Q390GNH specimen undergoes local corrosion that transforms into comprehensive corrosion. The reason for the difference is that the alloying elements of the two weathering steels are different. Q390GNH is added with a certain percentage of V and Ti, and higher Cr and Ni alloying elements hinder Cl⁻. The alloying elements of the two weathering steels in a later period are deposited to the inner rust layer to form a product film with a protective effect.

Keywords: Marine atmospheric environment; The salt fog corrosion test; Weathering steels; Alloy elements; Corrosion behavior

1. INTRODUCTION

The marine atmospheric environment is harsh and affected by high temperature, humidity, salt fog, radiation intensity and pollutant quantity[1-4]. In this environment, this phenomenon affects island equipment, reef equipment, metal products, etc. Severe corrosion leads to the failure of equipment materials[5-7].

As a material widely used in marine infrastructure construction, the atmospheric corrosion resistance of weathering steel is often 2 to 8 times higher than ordinary carbon steel[8]. Weathering steel often has different content ratios of alloying elements than ordinary carbon steel[9-11]. The rust layer generated due to the corrosion of the ocean atmosphere for a long period plays a protective role

in the substrate. Under some conditions, one can directly use bare steel without surface treatment[12]. To date, there are many studies on the corrosion of weathering steel from natural exposure to the ocean atmospheric environment[13-17], but there is little unique research on the corrosive behaviors that exist between different weathering steels.

When studying the problem of material corrosion in a marine atmospheric environment, it is inevitable to choose the applicable test method; due to the limitations of geographical locations and test cycles, natural exposure tests cannot be widely used[13, 18, 19]. In recent years, with the improvement and development of the experiment, the test cycle is short, and the influencing factors are controllable[20-23]. By assembling a reasonable indoor corrosion acceleration test, the experimental results of the experimental coupling of the natural exposure of the experiment are obtained in the short term. Therefore, it is easier to explore the corrosion behaviors and mechanisms of materials after long-term exposure. Cui[24] proposed that under a high-temperature and high-humidity environment, the effects of UV irradiation cause pitting corrosion, intergranular corrosion and exfoliation corrosion of materials; when the UV wavelength is different, the morphologies of corrosion products are different. Liu[25] studied the influence of environmental temperature and UV irradiation on the corrosion behavior of carbon steel in a tropical marine atmospheric environment and found that the composition and morphology of the rust layer changes with the environmental temperature and UV irradiation. To date, many studies have performed indoor acceleration corrosion experiments to study weather resistance[26-31]; the important factors of coupling ultraviolet radiation have less research on the corrosion process.

We select two types of weathering steel: Q295GNH and Q390GNH. Through multifactor coupling cycle acceleration experiments, weathering steels with different chemical components in interior acceleration and corrosion experiments with simulated ocean atmospheric environments are analyzed.

2. EXPERIMENT

2.1 Sample preparation

The experimental materials used were Q295GNH and Q390GNH produced by Dongguan Quansheng Special Steel Limited Company, and the specific chemical composition is shown in Table 1. The sample sizes were 20 mm × 20 mm × 5 mm for weight loss experiments, rust layer appearance observation, and rust layer analysis and 10 mm × 10 mm × 5 mm for electrochemical testing. All samples were polished with sandpaper to 1200#. After removing the oxidation layer and using acetone and dehydrated ethanol to remove the oxygen; the sample was dried with a hair dryer before being placed in a dry box for 24 h for later use.

Table 1. Chemical composition table of different weathering steels (wt.%).

Steel	C	Si	Mn	P	S	Cr	Ni	Cu	V	Ti	Mo
Q295GNH	0.12	0.18	0.31	0.008	0.002	0.15	0.18	0.22	-	-	-
Q390GNH	0.17	0.23	1.19	0.01	0.002	0.19	0.21	0.26	0.05	0.10	0.01

2.2 Experimental method

To simulate the corrosion of the sample in a real ocean atmospheric environment, a salt fog test box is used to simulate the erosion effect of Cl^- in the ocean atmospheric environment; the homemade accelerated corrosion test box simulates the influencing factors of ultraviolet radiation and dry and wet alternation. The experiments involve salt fog test, dry test and ultraviolet test. The experimental process of a single test cycle is shown in Table 2.

Table 2. Single cycle test flow and test parameters of the salt fog corrosion test.

Experimental step	Test duration (h)	Environmental parameter
Salt fog Test	8	Salt fog is 5% NaCl solution, temperature 35 °C
Dry test	4	Relative humidity 45% RH, temperature 25 °C
UV test	12	Radical strength 0.68 W/m ² , temperature 45 °C

The salt fog corrosion test is performed for a total of 18 cycles over 432 h, and they are sampled at 6 d, 9 d, 12 d, and 18 d.

2.3 Analysis of corrosion loss

The procedure of the corrosion loss test was as follows: first, the initial weight of the sample was determined by a precision electronic balance; then, the sample was removed at a corresponding sampling time and washed with a soft brush in running water; then, the sample was soaked for 10 min in a mixed solution of 500 mL hydrochloric acid (1.19 g/L), 3.5 g hexamethylenetetramine and 500 mL deionized water; then, the sample was cleaned ultrasonically for 10 minutes, dehydrated with water-free ethanol, dried in a blowing dryer, and finally placed in a dry box for 24 h. The weight of the sample was determined after removing the corrosion product. A weight loss analysis method was used to analyze the changes in the corrosion weight loss and corrosion rate of samples during different corrosion periods. The corresponding calculation formula was as follows:

$$w = \frac{m}{S} \quad (1)$$

$$v = 8.76 \times 10^4 \times \frac{m}{STD} \quad (2)$$

where w represents the corrosion weight (g/cm^2); m represents the weight loss (g); S represents the surface area (m^2); v represents the corrosion rate (mm/y); T represents the exposure time (h); and D represents the material density (g/cm^3).

2.4 Characterization of corrosion results

X-ray diffractometry (XRD) analysis was used for qualitative and semiquantitative analyses of the object phase under different corrosion cycles. The specific parameters were as follows: Cu target, K_{α} radial, 40 kV accelerating voltage, 40 mA current, 0.0167° /step scanning step size, 12 s residence time, and approximately 0.1° /min heat rate. Digital cameras and scanning electron microscopy (SEM) were used to observe the macro- and microappearance on the sample surfaces, respectively. The chemical component contents of corrosion products on the surfaces of samples under different corrosion cycles were analyzed by energy dispersive spectroscopy (EDS). The Gamry Electric Chemical Workstation was used to perform electrochemical analysis of the corrosive samples; this workstation is a three-electrode system with a platinum (PT) electrode as the auxiliary electrode, a saturated calomel electrode as the reference electrode and a weathering steel sample as the working electrode. The workstation was used to measure the dynamic polarization curve and electrochemical impedance spectroscopy (EIS) of the two weathering steels. For the polarization curve and electrochemical impedance spectrum (EIS), the test area was 1 cm^2 , the test frequency range was $100 \text{ kHz} \sim 0.01 \text{ Hz}$, and the amplitude was $\pm 0.01 \text{ V}$. For the linear polarization test, the scanning rate was 0.5 mV/s , and the scanning range was relative to the opening voltage of -0.5 V to $+1.5 \text{ V}$. All electrochemical tests were conducted in an electrolyte solution of 5 wt.% sodium chloride at room temperature (RT) of 25°C .

3. RESULTS AND ANALYSIS

3.1 Lost weight analysis

Figure 1 shows the loss and corrosion rates of Q295GNH and Q390GNH. Figure 1 (a) shows that with the increase in the number of experimental cycles, the corrosion of the two weathering steels increases, and the corrosion of the Q295GNH weathering steel is always higher than that of the Q390GNH weathering steel during the same cycle. After 12 days, the difference in corrosion reaches a maximum value. In Figure 1 (b), the corrosion rate of both weathering steels shows a decreasing trend. This phenomenon occurs because weathering steel adds alloying elements to generate the rust layer. In addition, the corrosion rate of Q390GNH weathering steel is always lower than that of Q295GNH weathering steel, which is directly related to their different chemical compositions. Some researchers have found that the addition of Cr improves the corrosion resistance of weathering steel, and the corrosion rate of weathering steel decreases with increasing test time[32]. The conclusion of this experiment is consistent with our results. From 6 days to 9 days, the decrease in the corrosion rate of Q295GNH weathering steel is significantly greater than that of Q390GNH weathering steel; from 9 to 12 days, the corrosion rate of Q295GNH weathering steel decreases slowly, and the corrosion rate of Q390GNH decreases more than that of Q295GNH weathering steel. After 18 days, the corrosion rate of Q390GNH decreases more gradually, while the corrosion rate of the Q295GNH weathering steel is relatively similar to the decrease in the previous stage.

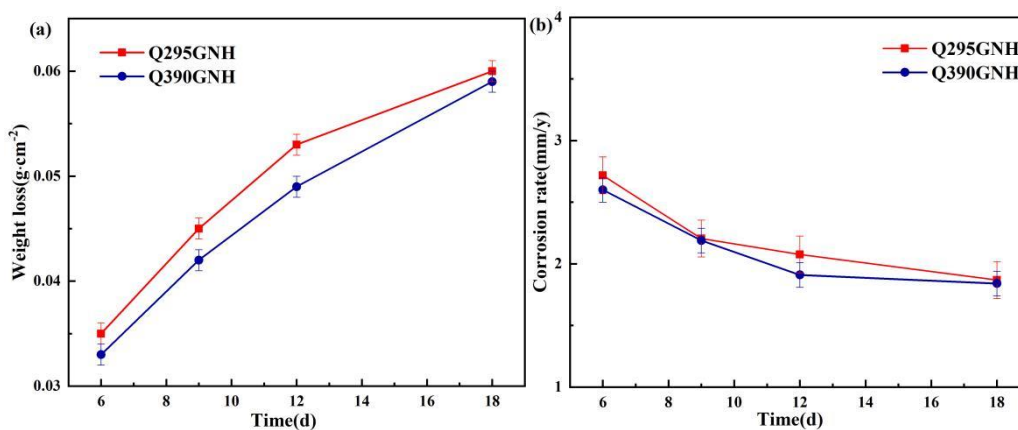


Figure 1. Corrosion loss (a) and corrosion rate (b) of two different weathering steels calculated by lost weight analysis after the salt fog corrosion test for different exposure times.

3.2 Model analysis

Figure 2 (a) and (b) show the macromorphologies of the Q295GNH and Q390GNH weathering steels, respectively. The figure shows that on the sixth day, the surface of the Q295GNH sample is covered by rust and there are local noncorrosive areas on the surface of the Q390GNH sample, indicating that the initial Q390GNH weathering steel has better corrosion resistance than Q295GNH. On the 12th day of the experiment, the brown–yellow rust layer formed by Q390GNH is loose, and the local rust layer falls off. Then, the dark brown rust layer is exposed with internal density and adhesive, explaining that at this time, Q390GNH forms a certain thickness and density rust layer; due to the defects and stress effects of local existence, the surface of the sample dips. On the 18th day, more dense dark brown corrosion products are generated, indicating that at this time, both weathering steels are generated with more protective rust layers.

Figure 3 shows the SEM images of Q295GNH and Q390GNH weathering steel under different trial cycles. Studies have shown that the corrosion rust layer of weathering steel is mainly composed of iron needle ore with a cotton ball structure (α -FeOOH), typical fine plates with flowery structures of lepidocrocite (γ -FeOOH), and typical cotton-ball and rosette morphologies of akaganeite (β -FeOOH). In addition, the α -FeOOH structure is more stable[33]. During the corrosion process, β -FeOOH and γ -FeOOH gradually change to α -FeOOH, forming a better-protected rust layer[32, 34]. By observing the microappearances of the Q295GNH and Q390GNH weathering steels, it is found that the corrosion products of the two types of steel in the early stages of corrosion are mainly composed of γ -FeOOH, as shown in Fig. 3 (a) and (e). Note that on the sixth day of the test, Q390GNH exhibits only local corrosion and generates a small amount of γ -FeOOH; some areas remain that are not corroded and exhibit little cracking. Generally, the surface of the corrosive appearance is relatively flat while the Q295GNH produces numerous γ -FeOOH during the same cycle; there are uneven areas on the surface, showing that Q295GNH enters the process of comprehensive corrosion. These phenomena prove that alloying elements, such as Cr, Ni, Ti, and V, exhibit certain impacts on its corrosive form and can effectively block the Cl⁻ from entering the surfaces of weathering steels in the early stage of corrosion.

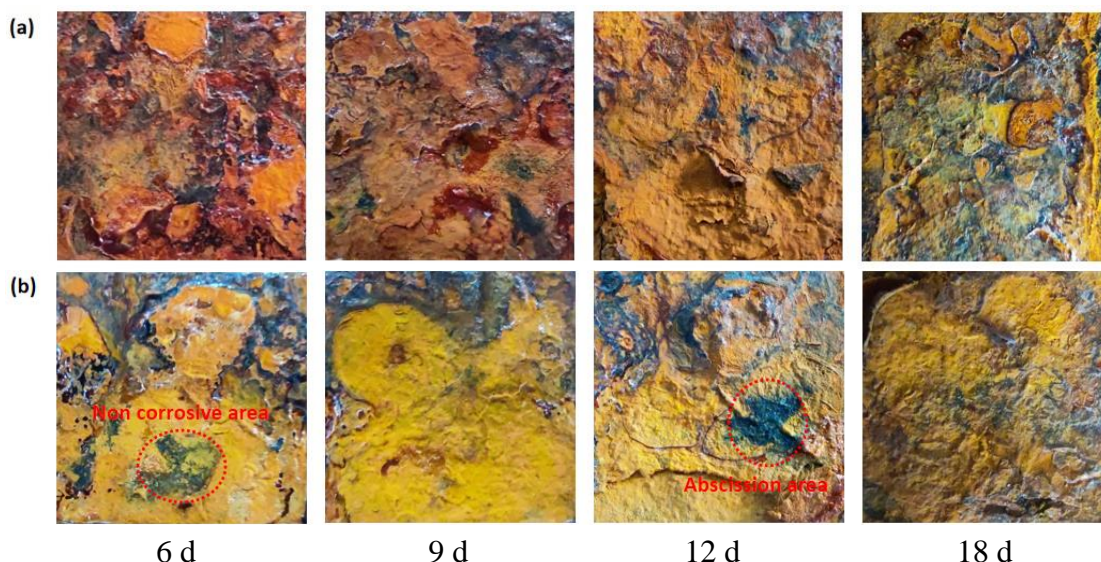


Figure 2. Morphological and surface corrosion damage analyses of Q295GNH (a) and Q390GNH (b) after the salt fog corrosion test under different exposure times (the steel surfaces were photographed with a digital camera).

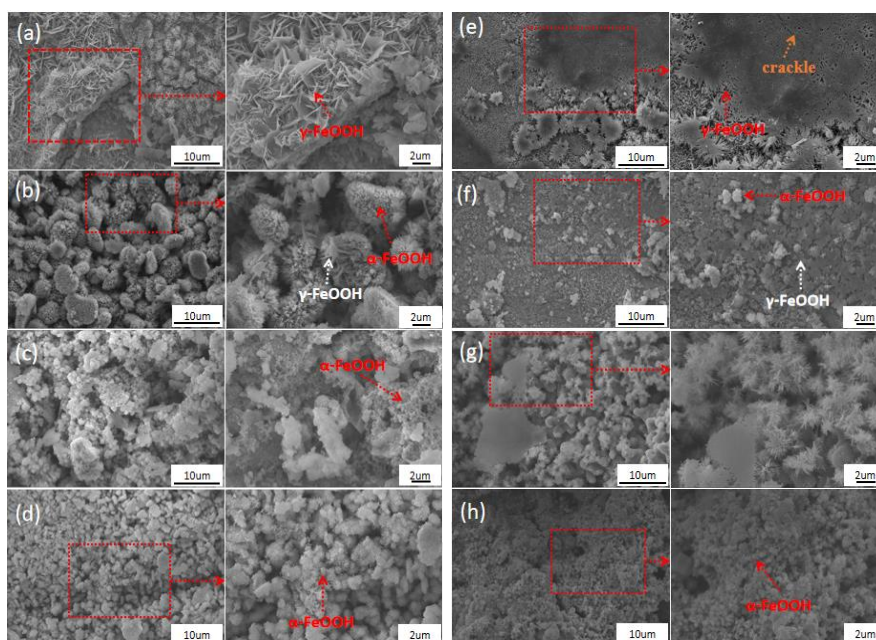


Figure 3. SEM images of Q295GNH (a–d) and Q390GNH (e–h) at different magnifications (1000 \times , 2000 \times) after the salt fog corrosion test for different exposure times: (a, e) 6 d; (b, f) 9 d; (c, g) 12 d; and (d, h) 18 d.

With the advancement of the test process, on the ninth day, the surface of Q295GNH initially forms more α -FeOOH. Most γ -FeOOH changes to α -FeOOH. The surface pores are large, and the rust layer is not dense enough, as shown in Fig. 3 (b). Moreover, the surface of Q390GNH, as shown in Fig. 3 (f), is basically corroded, and its corrosion products are gradually refined. There are more sliced

corrosion products and small amounts of transitional corrosion products in the forms of flocs and cotton balls, showing that the corrosion process is still slower than that of Q295GNH. On the 12th day of the test, there are still very few thin-sliced corrosion products and many needle-shaped cotton ball structures on the surface of Q390GNH. The surface is uneven and fragile, as shown in Fig. 3 (g), which is in line with the phenomenon observed in the corresponding macroscopic appearance at 12 days. In the later stage of the experiment, as shown in Fig. 3 (d) and (h), there are only fine and dense cotton balls and flocculent corrosion products on the surface of the two weathering steels, indicating that the corrosion product morphologies of the outer rust layers of the two weathering steels have transformed from thin plate shapes to cotton ball shapes. With the increase in the test cycle, cotton ball-like corrosion products are more refined and demented; eventually, a protective rust layer is formed. Song studied the corrosion behavior of Q345WS in different corrosion environments and found that steel changes from insignificant corrosion in the early stage to uniform corrosion and finally forms a dense protective corrosion film[35]. This conclusion is basically consistent with the corrosion behaviors of the Q295GNH and Q390GNH weathering steels. On the 18th day, the rust layer surface of Q390GNH is denser than that of Q295GNH, indicating that the addition of alloying elements not only affects the corrosion resistance of the weather resistance but also affects the density of the rust layer.

The differences between the alloying elements of the two weathering steels are mainly reflected in Cr, Ni, Ti, and V (the content of Mo is too low to measure). The alloying elements in the corrosion process can replace the Fe atoms in certain lattice positions and form spinel products or interstitial solid solutions to improve the corrosion resistance of materials[36, 37]. By analyzing the EDS results in Table 3, it is found that as the test cycle increases, the Cr and Ni contents of Q295GNH gradually decrease; Cr is not detected on the 18th day of the test, explaining that alloying elements, such as Cr and Ni, gradually deposit on and enrich the inner rust layer with the advancement of the corrosion process to promote the formation of the dense inner rust layer. Additionally, with the increase in the experimental cycle, the tip of the trial cycle first increases and then decreases. From the 9th day of the test, Q295GNH gradually forms a relatively dense outer rust layer, and Cr, Ni and other elements begin to enrich the inner rust layer. The EDS results of Table 4 show that the contents of V and Ti in Q390GNH decrease with the test cycle, Cr is not detected on the 9th day of the test; the regularity of the Ni content is not as obvious, indicating that when the elements are deposited in the inner rust layer, Cr is the most preferential, followed sequentially by V, Ti, and Ni. In addition, the Cl content is the highest on the 12th day (reaching 23.12 wt.%). According to Figure 5 (g), the rust layer is mainly composed of a long-cut cotton ball structure. This structure is the intermediate product formed by the transformation. Because the structural contact area is small, the pores are large, Cl⁻ easily attaches to the surface, the Cl content is high, and then the Cl content decreases; this finding indicates that after the test reaches the 12th day, the Q390GNH gradually forms a relatively dense outer rust layer.

Table 3. EDS results on the rust layer surface of Q295GNH after the salt fog corrosion test for different exposure times.

Test cycle (d)	Cr (wt.%)	Ni (wt.%)	Cl (wt.%)	Fe (wt.%)	O (wt.%)
6	0.05	0.04	1.6	74.61	23.70
9	0.01	0.04	2.67	68.56	28.72
12	0.07	0.04	0.57	75.78	23.54
18	0	0.03	0.21	73.36	26.4

Table 4. EDS results on the rust layer surface of Q390GNH after the salt fog corrosion test for different exposure times.

Test cycle (d)	Cr (wt.%)	Ni (wt.%)	Ti (wt.%)	V (wt.%)	Cl (wt.%)	Fe (wt.%)	O (wt.%)
6	0.08	0.01	0.02	0.04	1.18	85.56	13.11
9	0	0.16	0.01	0.02	1.15	67.21	31.45
12	0	0	0.01	0.07	23.12	47.05	29.75
18	0	0.04	0	0.03	1.28	75.03	23.62

3.3 Ingredient analysis

Figure 4 shows the composition of two weather-resistant rust layers after the cycle acceleration test. According to XRD analysis, the rust layers of Q295GNH and Q390GNH are composed of α -FeOOH, β -FeOOH, γ -FeOOH, and Fe_3O_4 . This finding is consistent with Fan's conclusion[9]. Figures 4 (a) and (b) show that the compositions of the two weathering steels are basically the same, but the corresponding peak intensities and widths of the two are different, indicating that the difference in chemical composition between different weathering steels affects the corrosion products generated. To analyze the differences more intuitively between the two corrosion products, we analyze the XRD results to determine the phase and α/γ^* ratios, as shown in Figure 6 (c) and (d). The figure shows that the proportion of α -FeOOH in Q295GNH and Q390GNH slowly increases with the increase in the number of test cycles, but the latter α -FeOOH proportion is significantly higher than the former. Since α -FeOOH has better stability than β -FeOOH and γ -FeOOH, as the test cycle increases, β -FeOOH and γ -FeOOH gradually become α -FeOOH, which further illustrates that Q390GNH has a higher anti-ocean corrosion ability than Q295GNH. In addition, Dillmann has proposed that the ratio of α/γ^* is often used to measure the tightness and protectiveness of the rust layer[38]. Among these parameters, α is used to measure the content of α -FeOOH in the rust layer, and γ is used to measure the total content of Fe_3O_4 and γ -FeOOH in rust layers[32]. The green points in Figures 4 (c) and (d) indicate the corresponding α/γ^* ratio. The figure shows that the ratio of α/γ^* for both Q295GNH and Q390GNH increases with increasing test cycles, indicating that with increasing test cycles, a denser rust layer forms on the surfaces of both weathering steels. Overall, the α/γ^* ratio of Q390GNH has always been higher than the ratio of Q295GNH, and it has been verified that Q390GNH has higher anti-maritime corrosion capabilities. Among the samples, Q295GNH does not change much when the test is at 9 d

and 12 d, indicating that during this cycle, Q295GNH forms a relatively dense outer rust layer that can block the immersion of most Cl⁻. This phenomenon is consistent with the morphology obtained from SEM images. Because the contents of Cr, Ni and other components of Q295GNH are lower than those of Q390GNH, and since the composition lacks alloying elements, such as Ti and V, it is easier to corrode at an initial stage of corrosion. Corrosion products are produced more rapidly, and the time required to form a dense rust layer is lower than that of Q390GNH. Therefore, the corrosion rate at the beginning of the test decreases faster than that of Q390GNH, which coincides with the results of Figure 1 b.

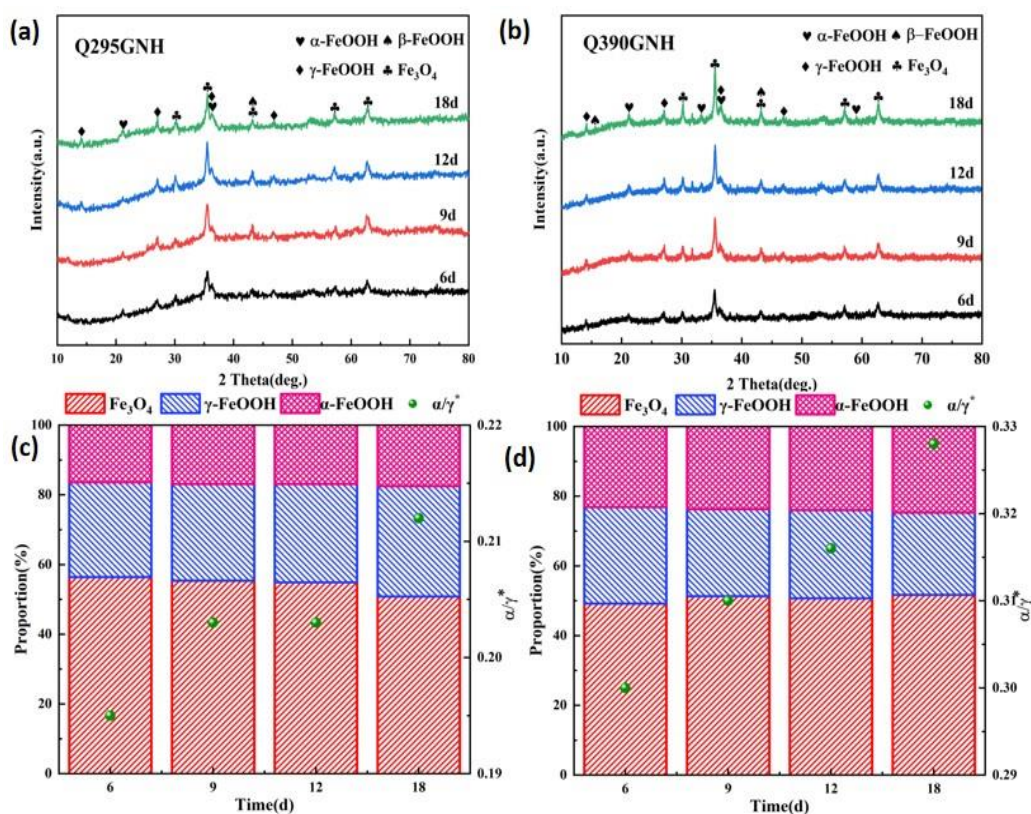


Figure 4. XRD patterns of corrosion products and proportions of various phases and α/γ^* ratios formed on Q295GNH and Q390GNH weathering steels after the salt fog corrosion test for different exposure times: (a) and (c) Q295GNH; (b) and (d) Q390GNH.

3.4 Electrochemistry

By conducting electrochemical tests in 5 wt.% NaCl solution, the corrosion resistance of two different weathering steels is determined. Figure 5 shows the dynamic polarization curves of the two different types of weathering steels. The figure shows that the corrosion potential of Q390GNH is higher than that of Q295GNH, showing that the corrosion resistance of Q390GNH is better than that of Q295GNH, which may be related to the high content of the relevant element in the Q390GNH chemical ingredients. When the weathering steel is immersed in a sodium chloride solution rich in Cl⁻, the anode preferentially undergoes the dissolution reaction of iron, while the cathode undergoes the

reduction reaction of oxygen and gradually form an iron oxide rust layer on the surface of weathering steel[39].

Table 5 shows the corrosion potential and corrosion current density of the two weathering steels under different test cycles. The table shows that the corrosion current densities of the two weathering steels after the acceleration test are higher than those of the samples that have not undergone the acceleration test, indicating that they have certain corrosion resistance. With the increase in the test days from 6 d to 9 d, the corrosion current densities of Q295GNH and Q390GNH decrease, indicating that the protective effect of the corroded rust layer gradually increases. In the conclusion drawn by Fan, it is proposed that the corrosion potential of weathering steel decreases negatively at the initial stage of corrosion, which is consistent with the conclusion of this paper[9]. Additionally, the variation in the corrosion current density of Q295GNH between each test cycle point is significantly less than that of Q390GNH. According to the SEM results analysis, the reason for this phenomenon is that Q295GNH itself is more easily corroded, and the time required to form a stable protective rust layer is less than that of Q390GNH. After the 6th day of the test, the stable corrosion product film formed can prevent the immersion of most Cl⁻, and the protection ability is close to saturation, which can explain why the corrosion current density of Q295GNH does not show a decreasing trend in the later stages of the test.

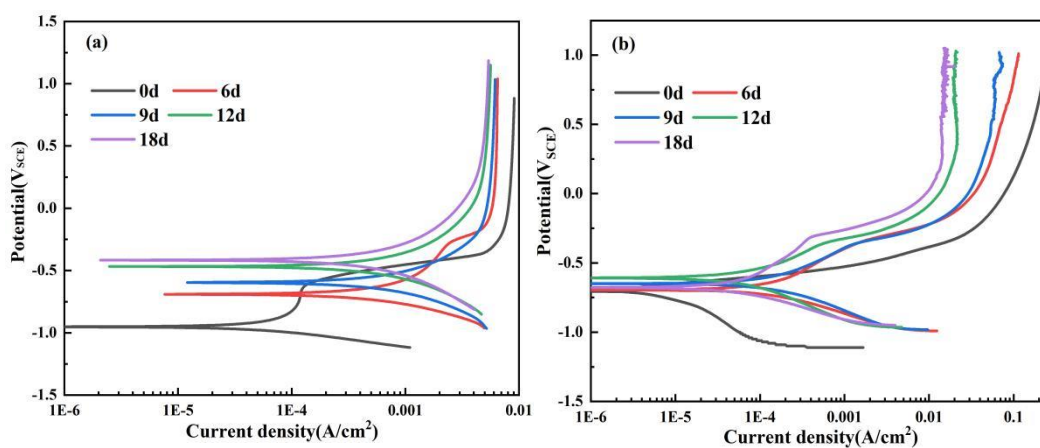


Figure 5. Polarization curves of Q295GNH (a) and Q390GNH (b) weathering steels in 5 wt.% NaCl solution after the salt fog corrosion test for different exposure times.

Table 5. Parameters of the electrochemical polarization for Q295GNH and Q390GNH steels in 5 wt.% NaCl solution after the salt fog corrosion test for different exposure times.

Test cycle (d)	Q295GNH		Q390GNH	
	<i>i</i> _{corr} (A cm ⁻²)	<i>E</i> _{corr} (V _{SCE})	<i>i</i> _{corr} (A cm ⁻²)	<i>E</i> _{corr} (V _{SCE})
0	8.253×10 ⁻⁵	-0.842	1.905×10 ⁻⁶	-0.696
6	7.625×10 ⁻⁴	-0.683	1.998×10 ⁻⁴	-0.694
9	6.288×10 ⁻⁴	-0.696	1.027×10 ⁻⁴	-0.649
12	7.035×10 ⁻⁴	-0.585	8.489×10 ⁻⁵	-0.608
18	6.794×10 ⁻⁴	-0.519	7.652×10 ⁻⁵	-0.677

To further explain the relationships of the corrosive product membranes between the two types of weathering steels, we gather EIS measurements of the weathering steel specimens. Figure 6 shows the Nyquist curves of the two different weathering steels. We easily find that the two weathering steels show similar capacitance behaviors[40]. Overall, the capacitance arc radii of the two weathering steels increase with increasing test cycles. Sun has tested two kinds of Cr advanced weather steels with different contents of Mo and has found that the capacitance arc radii of both steels increases with increasing immersion time, which is basically consistent with the conclusion of this paper[41]. From the low-frequency zone in Figure 6 (b) and (d), it can be seen that the capacitor arc radius of Q295GNH weathering steel increases with the increase in the test cycle, indicating that the protection of the corrosive rust layer gradually improves.

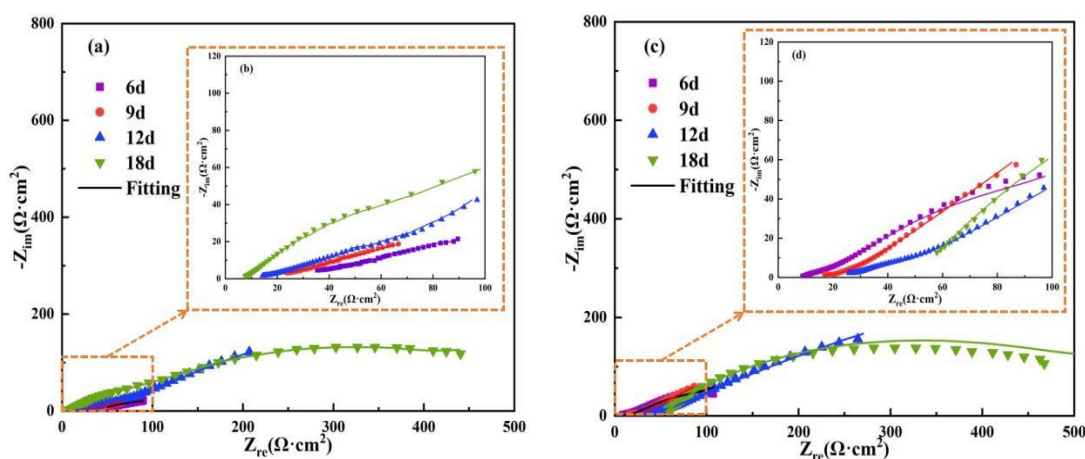


Figure 6. Electrochemical impedance spectra of Q295GNH and Q390GNH weathering steels in 5 wt.% NaCl solution after the salt fog corrosion test for different exposure times: (a) Nyquist plots of Q295GNH, (b) partial zoom diagram of Q295GNH, (c) Nyquist plots of Q390GNH and (d) partial zoom diagram of Q390GNH.

Q390GNH weathering steel shows the opposite change trend first and then gradually shows the same change law as Q295GNH, indicating that under the same test cycle, the corrosion product film generated by Q295GNH is more stable. The protection performance is better than that of Q390GNH, which is consistent with the experimental results obtained from the Tafel polarization curve. This finding shows the rationality of the EIS test.

Figure 7 shows the equivalent circuit diagram for the fitting results. R_s represents the solution resistance. Q_{p1} and R_{p1} represent the constant phase and resistance of the rust layer, respectively. Q_{d1} represents double-layer capacitors and R_{ct} represents the charge transfer resistance. Table 6 shows the partial fitting resistance and charge transfer resistance characteristics of the two types of weathering steels under different test cycles. For weathering steel, there is a connection between the thickness of the product membrane; thus, the fitting data can reflect the protection performance of the corrosive product membrane after the acceleration test. The table shows that the R_{ct} values of the two weathering

steels at 18 d of the test reach maximum values, showing that the corrosive membrane layer exhibits a protective effect on the substrate. Sun has found that the three fitting resistance characteristics in the equivalent circuit increases with the increase in the test period, and the resistance reaches its maximum value in the later stage of corrosion, which is consistent with the conclusion of this paper[41]. Additionally, the increase in the R_{ct} value from the 12th to the 18th day of the test for Q390GNH is significantly greater than that of Q295GNH. This finding suggests that more alloying elements of Q390GNH are deposited inward in the inner rust layer, enhancing the protection and denseness of the inner rust layer. This result is consistent with the EDS analysis results. In addition, we note that when tests at 6 d and 9 d are tested, the Q295GNH resistance transfer capacity is higher than that of Q390GNH, which may be related to the stability of the outer rust layer. There are cracks in the corrosive membrane layer, poor stability, and poor ability to obstruct Cl^- ; these results are consistent with the analysis results of EIS data. This phenomenon verifies the rationality of the fitting data.

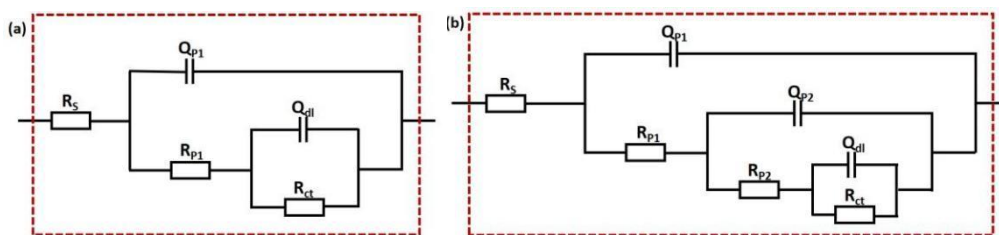


Figure 7. Equivalent circuit model of Q295GNH and Q390GNH weathering steels in 5 wt.% NaCl solution after the salt fog corrosion test for different exposure times: (a) the equivalent circuit model at 6 d and (b) the equivalent circuit model at 9, 12, and 18 d.

Table 6. Fitting parameters of the EIS for Q295GNH and Q390GNH weathering steels in 5 wt.% NaCl solution after the salt fog corrosion test for different exposure times.

Test cycle (d)	Q295GNH			Q390GNH		
	R_s	R_{p1}	R_{ct}	R_s	R_{p1}	R_{ct}
6	6.69	6.87	193.80	11.13	15.92	87.96
9	8.55	16.24	97.80	20.59	17.09	86.74
12	15.01	19.69	223.23	33.36	45.06	261.00
18	23.90	45.89	526.20	77.17	481.2	1292.00

4. DISCUSSION

Due to the high proportion of alloying elements in weathering steel, a protective corrosive rust layer can be generated in the ocean atmospheric environment. The rust layer is mainly composed of α -FeOOH, β -FeOOH, γ -FeOOH, and Fe_3O_4 [34]. When weathering steel is exposed to the atmosphere, it reacts with the water and oxygen in the air to generate $Fe(OH)_2$ first, and then the unstable $Fe(OH)_2$ is used as a reducing agent. O_2 in the air helps to further generate γ -FeOOH. γ -FeOOH is still not stable

enough. With the progression of corrosion, γ -FeOOH is converted into stable Fe_3O_4 or generated into α -FeOOH through a solid phase change[32]. The specific chemical equation is as follows:



Based on the above discussions and analyses, Q295GNH and Q390GNH have different corrosion mechanisms and laws during the corrosion process due to their different chemical compositions, as shown in Figure 8.

4.1 Q295GNH weathering steel corrosion mechanism

In the early stages of corrosion, as shown in Figure 8 (a), a large amount of γ -FeOOH is generated on the surface of the Q295GNH weathering steel. A small amount of γ -FeOOH is transformed into stable α -FeOOH. Fan has proposed that the influence of Cl^- on corrosion resistance is mainly related to its concentration[34]. A large amount of Cl^- in the air uses the cracks and holes in the rust layer to pass through the layer and continue to erode the matrix material. At this time, Cr and Ni are not deposited or evenly distributed in the rust layer. Some studies suggest that with the increase in Ni content, the rust layer produced by weathering steel becomes smoother, and the porosity decreases so that they effectively block the penetration and precipitation of chloride ions[42]. For Q295GNH, the Ni content is low, and only a small amount of Cl^- is blocked by Cr and Ni. Thus, the specimen soon enters the uniform corrosion stage, and the corrosion rate is large. When entering the postcorrosion period, as shown in Figure 8 (b), most γ -FeOOH is converted to α -FeOOH; additionally, the inner rust layer becomes denser, and most Cl^- is blocked outside the inner rust layer. At this time, Cr and Ni are deposited into the inner rust layer, and a small part of Cl^- is blocked by Cr and Ni enriching the inner rust layer. The elements cannot be exposed to the substrate material. Therefore, the corrosion rate gradually decreases, thereby protecting the substrate material.

4.2 Q390GNH weathering steel corrosion mechanism

In the early stages of corrosion, as shown in Figure 8 (c), the Q390GNH weathering steel first generates γ -FeOOH and a small amount of α -FeOOH. This result is consistent with previous conclusions showing that after short-term exposure, the main phase is amorphous or crystalline hydroxyl oxides[43]. Due to the addition of higher contents of Cr, Ni and certain proportions of V and Ti-based alloying elements in Q390GNH, the base material is prevented from entering the base material when corroded by Cl^- . This phenomenon is consistent with Zhang's conclusion that an increase in the Cr content can reduce the corrosion rate of weathering steel[44]. However, the density of the rust layer is still insufficient, and a small part of Cl^- contacts the matrix material through cracks and holes. Therefore, the early corrosion degree is lighter than that of Q295GNH, and local corrosion only occurs at the initial stage. At the later stage of corrosion, as shown in Figure 8 (d), the corrosion

process of the substrate material gradually changes from local corrosion to comprehensive corrosion. The decline in the corrosion rate remains at a high level. However, as the test continues, the composition of the inner rust layer is mainly a large amount of α -FeOOH, and all alloying elements are gradually deposited on the inner rust layer[9]. Cl⁻ does not continue to erode the matrix material. The compactness of the inner rust layer is further increased, and the downward trend of the corrosion rate is significantly decelerated, thus protecting the substrate.

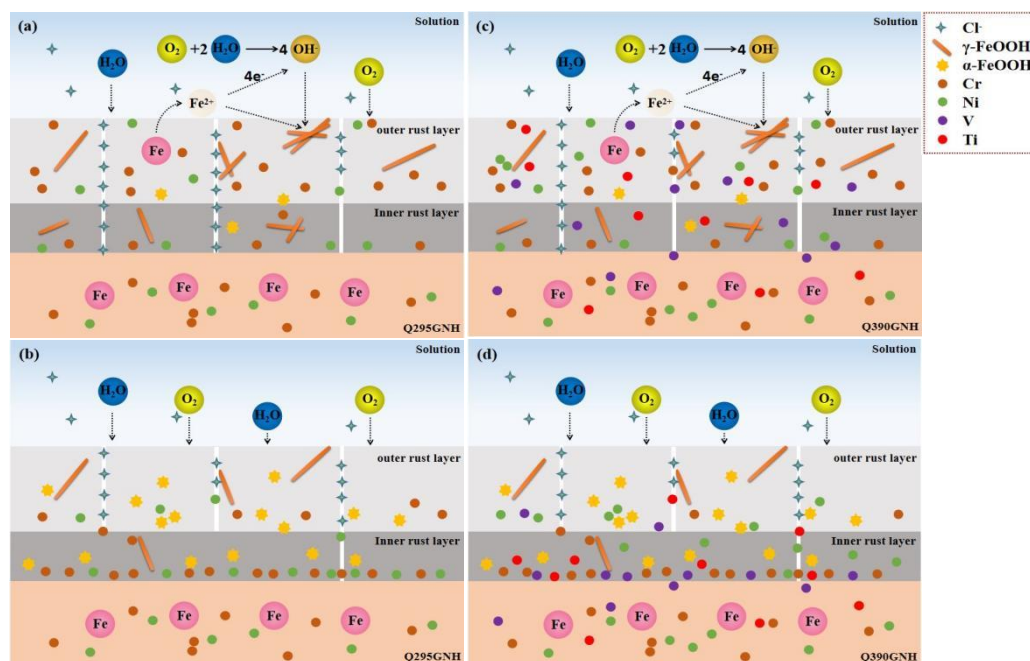


Figure 8. Schematic diagram of the corrosion mechanisms of two weathering steels: (a) and (b) Q295GNH; (c) and (d) Q390GNH.

5. CONCLUSION

The salt fog corrosion test is used to study the differences between Q295GNH and Q390GNH weathering steels in the simulated ocean atmospheric environment. The following conclusions are obtained from the research results:

(1) During the 18 d test cycle, the erosion loss and corrosion rates of Q295GNH are always higher than those of Q390GNH, but there are differences in the changes in the corrosion rates. Q295GNH's corrosion rate decreases dramatically before testing at 9 d and then decelerates. The downward trend of the corrosion rate of Q390GNH is more stable before 9 d of testing and larger between 9 d and 12 d than Q295GNH. Finally, the corrosion rate decreases gradually. The corrosion rates of the Q295GNH and Q390GNH weathering steels are close at 1.868 mm/y and 1.840 mm/y, respectively, after 18 d of testing.

(2) The corrosion products of Q295GNH and Q390GNH are composed of α -FeOOH, β -FeOOH, γ -FeOOH, and Fe₃O₄. Q295GNH is more likely to be corroded; after 6 days of testing, it

enters the stage of uniform corrosion. The corrosion process of Q390GNH gradually changes from local to comprehensive corrosion.

(3) The differences between the chemical compositions of the two weathering steels mainly affect the corrosion resistance of the base material in the early stage of corrosion. Entering the late corrosion, the alloying elements of the two weathering steels are deposited on the inner rust layer, which prevents Cl⁻ erosion. After enough corrosion cycles, the corrosion product films of both play protective roles in marine and atmospheric environments.

ACKNOWLEDGEMENT

This work was supported by Open Fund (PLN2022-47) of State Key Laboratory of Oil and Gas Reservoir Geology and Exploitation (Southwest Petroleum University).

References

1. I.S. Splavskiy, *J. Mach. Manuf. Reliab.*, 50(2021)319.
2. N. Li, W.F. Zhang, H.Xu, Y.K. Cai and X.J. Yan, *Materials (Basel, Switzerland)*, 15(2022)629.
3. Z.Y. Liu, W.K. Hao, W. Wu, H. Luo and X.G Li, *Corros. Sci.*, 148(2019)388.
4. X.Y. Zhang, M. Liu, F. Lu, M.H. Liu, Z.H. Hua and Z.H.Tang, *Corros. Sci. Technol.*, 17(2018)6.
5. B.J. Dong, W. Liu, T.Y. Zhang, L.J. Chen, Y.M. Fan, Y.G. Zhao, W.J. Yang and W. Banthukul, *Eng. Fail. Anal.*, 129(2021)105720.
6. W. Xue, Z.H. Li, W. Yu, C.F. Dong, X.G. Li and K. Xiao, *J. Iron Steel Res. Int.*, 31(2019)296.
7. W. Chen, K. Wang, X. Liu, N.R. He, H. Xin and W.H. Hao, *Int. J. Refract. Met. H.*, 81(2019)345.
8. M. Morcillo, B. Chico, I. Díaz, H. Cano and D. de la Fuente, *Corros. Sci.*, 77(2013)6.
9. Y.M. Fan, W. Liu, S.M. Li, T. Chowwanonthapunya, W. Banthukul, Y.G. Zhao, B.J. Dong, T.Y. Zhang and X.G. Li, *J. Mater. Sci. Technol.*, 39(2020)190.
10. M. Morcillo, I. Díaz, H. Cano, B. Chico and D. de la Fuente, *Constr. Build. Mater.*, 213(2019)723.
11. M. Morcillo, I. Díaz, H. Cano, B. Chico and D. de la Fuente, *Constr. Build. Mater.*, 222(2019)750.
12. P.F. Lin, Z. Yang, Y. Chen and Z. Li, *Kang T'ieh/Iron and Steel*, 56(2021)58.
13. Y. Feng, Z. Bai, L. Chen, D. Wei, D. Zhang, Q. Yao, J. Wu, C. Dong and K. Xiao, *J. Chin. Soc. Corros. Prot.*, 39(2019)519.
14. D. Cheng, J. Zhao, B. Liu, C. Jiang, X. Fu and X. Cheng, *J. Chin. Soc. Corros. Prot.*, 39(2019)29.
15. X.Y. Guo, J.F. Kang, J.S. Zhu and M.H. Duan, *J. Mater. Civ. Eng.*, 31(2019)9.
16. R.E. Melchers, *Corros. Sci.*, 50(2008)3446.
17. P. Tao, J.Q. Sun, C.C. Dong, H.Y. Yang and B. Zhang, *Equipment Environmental Engineering*, 14(2017)21.
18. T.G. Duan, L.K. Xu, K.K. Ding, W.S. Peng, J. Hou, W.M. Guo and W.H. Cheng, *Corros. Sci. Technol.*, 54(2019)485.
19. X.D. Zhao, G.F. Xi and J. Yang, Mechanical, *Materials and Manufacturing Engineering*, PTS 1-3, 66-68(2011)1828.
20. K. Woloszyk, Y. Garbatov, and J. Kowalski, *Ocean Eng.*, 241(2021)110039.
21. C.X. Huang, X.H. Su, Q.Q. Song and X.D. Wang, *Anti-Corros. Methods Mater.*, 68(2021)564.
22. Y.C. Liang, M. Nie, W.L. Zhong, J.D. Lin, C.L. Dong, Y.T. Ma and Y. Li, *Corros. Sci. Prot. Technol.*, 28(2016)337.
23. M. Liu, X.Q. Cheng, X.G. Li and J.Z. Hu, *Case Stud. Constr. Mater.*, 5(2016)87.
24. Y.Y. Cui, Y.N. Gao, Y.X. Qin and X.Y. Shi, *Int. J. Chem. Eng.*, 2021(2021)1.
25. Y.W. Liu, M.R. Liu, X. Lu and Z.Y. Wang, *Mater. Chem. Phys.*, 277(2022)124962.
26. W. Wu, Z.P. Zeng, X.Q. Cheng, X.G. Li and B. Liu, *J. Mater. Eng. Perform.*, 26(2017)6075.

27. L.H. Gong, Q. Xing and H.H. Wang, *Anti-Corros. Method. M.*, 63(2016)1.
28. P.P. Zhang, Z.M. Yang, Y. Chen and H.M. Wang, *J. Chin. Soc. Corros. Prot.*, 37(2017)93.
29. G.Q. Fu, D.L. Li and M.Y. Zhu, *Kang T'ieh/Iron and Steel*, 53(2018)94.
30. C. Wang, G.W. Cao, C. Pan, Z.Y. Wang and M.R. Liu, *J. Chin. Soc. Corros. Prot.*, 36(2016)39.
31. X.Y. Guo, J.S. Zhu, J.F. Kang, M.H. Duan and Y.G. Wang, *Constr. Build. Mater.*, 234(2020)117393.
32. M.H. Sun, C.W. Du, Z.Y. Liu, C. Liu, X.G. Li and Y.M. Wu, *Corros. Sci.*, 186(2021)109427.
33. F.R. Pérez, C.A. Barrer, K.E. García, *Corros. Sci.*, 52(2010)2582.
34. Y.M. Fan, W. Liu, Z.T. Sun, T. Chowwanonthapunya, Y.G. Zhao, B.J. Dong, T.Y. Zhang and W. Banthukul, *Constr. Build. Mater.*, 266(2021)120937.
35. Z.T. Song, T.M. Guo and Y.W. Zhang, *Surf. Topogr. Metrol. Prop.*, 8(2020)025004.
36. R.H. McCuen and P. Albrecht, *J. Mater. Civ. Eng.*, 17(2006)117.
37. C.H. Song, X.J. Zhou, J.Z. Li, F. Huang, Z.H. Gan and R. Wu, *Mater. Mech. Eng.*, 36(2012)62.
38. Ph. Dillmann, F. Mazaudier and S. Hœrlé, *Corros. Sci.*, 46(2004)1401.
39. Z.H. Wang, X. Zhang, L. Cheng, J. Liu and K.M. Wu, *J. Mater. Res. Technol.*, 10(2021)306.
40. J.H. Jia, X.Q. Cheng, X.J. Yang, X.G. Li and W. Li, *Constr. Build. Mater.*, 259(2020)119760.
41. M.H. Sun, Y.J. Pang, C.W. Du, X.G. Li, and Y.M. Wu, *Constr. Build. Mater.*, 302(2021)124346.
42. F.Z. Liu, *Int. J. Electrochem. Sci.*, 16(2021)151017.
43. Juan A. Jaén, Josefina Iglesias and Cecilio Hernández, *Int. J. Corros.*, 2012(2012)11.
44. W.H. Zhang, S.W. Yang, W.T. Geng, Q. Hu and L.J. Zhou, *Mater. Chem. Phys.*, 288(2022)126409.

© 2022 The Authors. Published by ESG (www.electrochemsci.org). This article is an open access article distributed under the terms and conditions of the Creative Commons Attribution license (<http://creativecommons.org/licenses/by/4.0/>).